Operating characteristics of a femtosecond amplification cavity for infrared frequency combs

J. T. Chia, S. E. Martin, D. R. Carlson, R. J. Jones, and E. M. Wright
College of Optical Sciences, The University of Arizona, Tucson, Arizona 85721, USA
(Received 27 September 2012; published 15 February 2013)

We develop a cavity model including transverse field variations and gain saturation to elucidate the operating characteristics of a femtosecond amplification cavity (fsAC) with an incident infrared frequency comb. After validating the model against experimental data, we explore how the fsAC operating characteristics, such as average output power and beam quality, vary with factors such as the pump beam and the output coupler reflectivity. We also examine the locking range of the fsAC and how the nonlinear Kerr effect places a limitation on the pulse duration that can be successfully amplified by the fsAC.

DOI: 10.1103/PhysRevA.87.023817 PACS number(s): 42.60.Da, 42.55.Ah, 42.60.Jf, 42.60.Lh

I. INTRODUCTION

Stable mode-locked laser systems such as the femtosecond frequency comb are often limited in their high power operation due to temporal instabilities resulting from high peak intensities. External amplification of the pulse train to higher average powers at the full repetition rate of the laser is typically inefficient for bulk solid-state systems due to low gain and short interaction lengths that result from the need for tightly focused pump beams. In previous work, we demonstrated the use of optical injection locking with femtosecond pulse trains as an approach to scale up the average power of Ti:sapphire-based fs frequency combs to record power levels [1]. Although similar to many cw injection-locking schemes, one must also take into account the additional parameters of pulse phase, timing, and nonlinear effects in designing the femtosecond amplification cavity (fsAC). The high average powers that could be obtained in the Ti:sapphire-based system were used by our group to significantly increase the power in a VUV frequency comb based on intracavity high-harmonic generation [2]. The fsAC approach enables flexibility for many applications by enabling coherent amplification of the entire, or *portions* of the, broad master laser spectrum. Furthermore, one could envisage intracavity experiments with interactions which would otherwise be too lossy to be performed in a passive fs enhancement cavity (fsEC) alone.

In our initial work, we demonstrated that operation of the fsAC is in many ways similar to that of cw injection locking, provided the incident pulse train is sufficiently chirped to reduce the pulse peak intensity and both the pulse train timing and phase (i.e., two degree's of freedom) are appropriately stabilized to the fsAC. In this paper, we begin to explore in more detail the operating characteristics of the fsAC over a broader range of operating parameters to enable predictive performance for a greater variety of potential applications. We focus here on aspects of the cavity design that affect the expected power levels as well as the effective locking range for the fsAC. In future work, we will report on an extension of this model to take into account the temporal structure of the pulse train and the effects of dispersion on the performance of the fsAC.

II. THE FEMTOSECOND AMPLIFICATION CAVITY

The experimental setup is shown schematically in Fig. 1. The Ti:sapphire ring laser cavity is initially aligned and optimized for maximum output power and beam quality. In this free-running mode (i.e., not injection locked), the fsAC output is bidirectional and multimode. When locked to an incident Ti:sapphire pulse train, the output becomes unidirectional and assumes the same spectral and temporal properties as the master oscillator. This locking is accomplished using the Pound-Drever-Hall technique by modulating a small piezoelectric transducer mounted to a cavity mirror. Further details of the system are found in Ref. [1]. For the pulse bandwidths considered in the previous work and again analyzed here, there was no noticeable limiting effect on the operation of the fsAC deriving from the residual group-delay dispersion of the cavity. As a result, the model presented here does not include dispersion-related effects and the pulse stretching and compression features [including an intracavity prism pair for group delay dispersion (GDD) compensation] have been omitted from the figure. The Ti:sapphire-crystal mount is cooled using a thermoelectric cooler to near 0 °C; however, the intense 18 W pump beam induces some local heating in the crystal. Because we operate at power levels where pump-beam-induced thermal lensing only begins to limit the fsAC performance, we exclude such effects in our model. Although thermal limitations would prevent the operation of our current fsAC design at high powers, such effects can be, and have previously been, mitigated by improved cooling of the Ti:sapphire rod.

The specific fsAC cavity we consider has a distance $d = 10.1$ cm between the curved mirrors of equal radius of curvature $R = 10$ cm, the curved mirrors are rotated by an angle of 5°, and the round-trip path length is $L = 3$ m. We consider a reference plane that is halfway between the curved mirrors at the position of the Ti:sapphire gain medium. Using these parameters, the ray transfer matrices with elements A_x, B_x, C_x, D_x and A_y, B_y, C_y, D_y along the sagittal and tangential planes of the cavity are readily evaluated and the corresponding complex beam parameters $q_{x,y}$ of the Gaussian mode along the respective transverse dimensions are calculated for the center wavelength of $\lambda = 0.8$ μm [3]. For our choice of reference plane, the Gaussian mode is focused and has nearly equal spot sizes, $w_x \simeq w_y \simeq 15$ μm. That is, the Gaussian mode has little astigmatism at the reference plane.

The above fsAC cavity corresponds to a $f_{\text{rep}} = 100$ MHz repetition rate. We also consider a $f_{\text{rep}} = 50$ MHz fsAC that includes a 3 m intracavity telescope section so that the ray transfer matrices, and hence the Gaussian-mode properties,

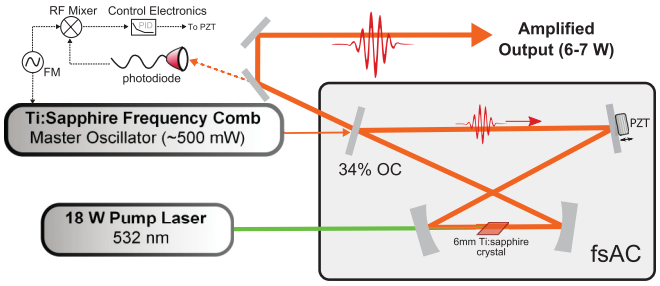

FIG. 1. (Color online) Simplified schematic of the fs amplification cavity. The fsAC is seeded by a low-power Ti:sapphire frequency comb and is locked to it by modulating a piezoelectric transducer (PZT) mounted to a cavity mirror. As dispersion effects have been neglected in this treatment, an intracavity prism pair for group-delay dispersion compensation has been omitted.

are the same as for the 100 MHz case despite the on-axis path length being twice as long.

III. MODEL EQUATIONS

The goal of this paper is to simulate many of the basic operating characteristics of a fsAC. In this section, we describe the model equations employed for our simulations and the underlying assumptions. In particular, we employ a model that neglects cavity dispersion and thus does not treat the temporal dynamics in detail. However, we find that in order to obtain agreement with experimental data, we need to account for the transverse structure of the medium gain profile.

A. Cavity field equations

In the experiment, the pulses comprising the incident frequency comb centered at $\lambda = 0.8\ \mu$m are expanded to a duration of t_p before entering the fsAC. We neglect the effects of dispersion within the cavity and assume that the incident pulse train may be adequately modeled as a sequence of square pulses of duration t_p, *average* incident power $P_{\rm in}$, and repetition rate $f_{\rm rep} = 1/T$, with $T \gg t_p$ being the fsAC round-trip time. The incident pulse train therefore synchronously pumps the cavity. We further assume that the incident field is mode matched to the Gaussian mode of the cavity, which has a focused spot size of $w_0 \simeq 15\ \mu$m at the longitudinal position of the gain medium. The incident field profile at the position of the gain medium is thus of the form $E(x,y) \propto \exp[-(x^2+y^2)/w_0^2]$, with (x,y) the transverse coordinates perpendicular to the laser axis. For the experiments, the gain medium has a length $L = 6$ mm and the Rayleigh range of the cavity mode is $z_R = n_0 \pi w_0^2/\lambda \simeq 15$ mm, with $n_0 = 1.76$ at $\lambda = 800$ nm. Since $z_R > L$, we shall treat the Ti:sapphire medium as a thin gain sheet and ignore diffraction within the gain medium.

Under the above assumptions, we describe the cavity field using the slowly varying complex amplitude $E^{(n)}(x,y)$ after n round trips, where $|E^{(n)}(x,y)|^2$ is normalized such that it yields the transverse fluence profile $J^{(n)}(x,y)$ of the pulse circulating in the cavity. Here we consider a reference plane just before the gain medium where the cavity-mode spot size is w_0. In a similar manner, the complex field representing the input pulse just before the gain medium may be written as

$$E_{\rm in}(x,y) = \sqrt{\frac{2P_{\rm in}}{\pi w_0^2 f_{\rm rep}}}\, e^{-(x^2+y^2)/w_0^2}. \tag{1}$$

Building on the above discussion, the circulating field $E^{(n+1)}(x,y)$ after $(n+1)$ round trips, and just before the gain medium, may be related to that after n round trips using the mapping

$$E^{(n+1)}(x,y) = re^{i\phi}\hat{K}[\sqrt{G^{(n)}(x_0,y_0)}E^{(n)}(x_0,y_0)] + tE_{\rm in}(x,y), \tag{2}$$

where $r = \sqrt{R}$ and $t = i\sqrt{1-R}$ are the field reflection and transmission coefficients of the output coupler of reflectance R, ϕ is an on-axis round-trip phase shift (see below), and $G^{(n)}(x_0,y_0)$ is the net power gain profile after n round trips that we describe in Sec. III B. The cavity mapping in Eq. (2) may be interpreted as follows: The field $E_n(x_0,y_0)$ over the transverse plane (x_0,y_0) just before the gain medium is first multiplied by the field gain profile $\sqrt{G^{(n)}(x_0,y_0)}$ to account for amplification. The integral operator $\hat{K}$ then propagates the field exiting the gain medium around the cavity. More specifically, for an initial function $F(x_0,y_0)$, the integral operator produces an output $H(x,y)$ according to the generalized Huygens integral for the cavity [4], where

$$\begin{aligned} H(x,y) &= \hat{K}[F(x_0,y_0)] \\ &= \frac{1}{i\lambda\sqrt{B_xB_y}}\int\!\!\int_{-\infty}^{\infty} dx_0dy_0 e^{\frac{ik_0}{2B_x}[A_xx^2-2xx_0+D_xx_0^2]} \\ &\quad \times e^{\frac{ik_0}{2B_y}[A_yy^2-2yy_0+D_yy_0^2]}F(x_0,y_0). \end{aligned} \tag{3}$$

Once we have the propagated field $\hat{K}[\sqrt{G^{(n)}}E^{(n)}]$, we need to multiply it by $re^{i\phi}$ to account for reflection of the output coupler and the round-trip phase shift, and add on the incident field transmitted through the output coupler, with the result being the circulating field $E^{(n+1)}(x,y)$ after $(n+1)$ round trips.

The round-trip phase shift ϕ accounts for the fact that the input frequency may not exactly match a cavity mode. In particular, the Gaussian mode accumulates a net phase shift per round trip given by

$$\phi_G = \arg\left(\frac{1}{\sqrt{(A_x+B_x/q_x)(A_y+B_y/q_y)}}\right), \tag{4}$$

where $q_{x,y}$ are the complex beam parameters along the two transverse directions. For our case in which the reference plane is chosen at the gain medium, we have $\frac{1}{q_{x,y}} = \frac{2i}{kw_0^2}$. The round-trip phase shift is then written in the form

$$\phi = -\phi_G + \phi_L, \tag{5}$$

so that the term $-\phi_G$ negates the Gaussian beam phase shift and ϕ_L is then the phase shift due to detuning of the fsAC length from the on-resonance condition. Unless otherwise stated, we take the resonant case with $\phi = -\phi_G$. (In Sec. V, we shall allow for detuning to investigate the locking range of the fsAC along with a nonlinear extension to account for the Kerr effect.)

For the simulations, we iterate Eq. (2) for the internal field starting from $E^{(0)}(x,y) = 0$ to find the steady-state solution $E^{(n+1)}(x,y) = E^{(n)}(x,y) = E(x,y)$ for the cavity field, which

is then used to extract the operating characteristics of the fsAC. (Non-steady-state solutions will be relevant in Sec. V with respect to the locking range of the fsAC.) Of particular interest here is the average output power of the pulse train exiting the fsAC. To calculate the output power, we need to obtain the output field $E_{\rm out}(x,y)$ at the output coupler from the steady-state field $E(x,y)$. To this end, it is useful to write the integral operator in Eq. (3) in the form $\hat{K} = \hat{K}_{or}\hat{K}_{ro}$, where $\hat{K}_{ro}$ is the integral operator for field propagation from the reference plane at the gain medium to the output coupler starting out propagating to the right, and $\hat{K}_{or}$ is the integral operator that performs free-space diffraction from the output coupler to the reference plane at the gain medium. The field at the output coupler may then be expressed formally as

$$E_{\rm out}(x,y) = te^{i\phi}\hat{K}_{ro}[\sqrt{G(x_0,y_0)}E(x_0,y_0)] + r\hat{K}_{or}^{-1}[E_{\rm in}(x_0,y_0)], \tag{6}$$

so that the fluence profile at the output will be given by $J_{\rm out}(x,y) = |E_{\rm out}(x,y)|^2$, and the average output power is

$$P_{\rm out} = f_{\rm rep}\int_{-\infty}^{\infty}\int_{-\infty}^{\infty} dxdy|E_{\rm out}(x,y)|^2. \tag{7}$$

We remark that the steady-state solution represented by Eqs. (6) and (7) should correspond to an output pulse train, or infrared frequency comb, whose average power is amplified with respect to the input pulse train, but with otherwise identical pulse duration t_p and repetition rate $f_{\rm rep}$.

Equations (6) and (7) are not particularly practical, but one can use them to access the output power in a simpler manner. In particular, if one operates on both sides of Eq. (6) with $\hat{K}_{or}$, we obtain

$$\tilde{E}_{\rm out}(x,y) = K_{or}[E_{\rm out}(x_0,y_0)] = te^{i\phi}\hat{K}[\sqrt{G(x_0,y_0)}E(x_0,y_0)] + rE_{\rm in}(x,y). \tag{8}$$

Now, although the field $\tilde{E}_{\rm out}(x,y)$ is not referenced to the output coupler, its norm will be the same as $E_{\rm out}(x,y)$ since the operator $\hat{K}_{or}$ represents free-space diffraction which preserves the norm of the field, so the output power is obtained in equivalent form as

$$P_{\rm out} = f_{\rm rep}\int_{-\infty}^{\infty}\int_{-\infty}^{\infty} dxdy|\tilde{E}_{\rm out}(x,y)|^2. \tag{9}$$

Thus, once we have the steady-state internal field $E(x,y)$, we calculate $\tilde{E}(x,y)$ using Eq. (8) and finally the average output power $P_{\rm out}$ using Eq. (9).

B. Gain model

So far we have introduced the net power gain as $G^{(n)}(x,y)$. To proceed, we write the net power gain after n round trips as $G^{(n)}(x,y) = \exp[g^{(n)}(x,y)]$, with $g^{(n)}(x,y)$ the gain. Within the usual four-level model for a Ti:sapphire laser medium, the gain $g^{(n)}(x,y)$ will be proportional to the upper lasing level population. We consider a Gaussian pump beam of spot size w_p resulting in a Gaussian profile for the small-signal gain in the absence of gain saturation,

$$g_s(x,y) = g_0 e^{-2(x^2+y^2)/w_p^2}, \tag{10}$$

where g_0 will be proportional to the peak intensity of the pump beam. To incorporate the effects of gain saturation and propagation in the Ti:sapphire medium, we employ the Frantz-Nodvik model [5] generalized to allow for gain recovery between pulses,

$$g^{(n+1)}(x,y) = g^{(n)}(x,y) - \frac{J^{(n)}(x,y)}{J_{\rm sat}}\left[e^{g^{(n)}(x,y)} - 1\right] + \frac{[g_s(x,y) - g^{(n)}(x,y)]}{f_{\rm rep}\tau}. \tag{11}$$

Here $g^{(n)}(x,y)$ is the gain profile after n round trips, $g^{(0)}(x,y) = g_s(x,y)$, $J_{\rm sat}$ is the saturation fluence, τ is the lifetime of the upper state lasing transition, and $J^{(n)}(x,y) = |E^{(n)}(x,y)|^2$ is the pulse fluence profile after n round trips. The top line of this equation corresponds to the Frantz-Nodvik model in the form previously applied to regenerative amplification in Ti:sapphire media [6]. In contrast, the second line corresponds to the gain recovery that occurs in the time interval $T = 1/f_{\rm rep}$ between successive pulses. We note that in the absence of an intracavity field, $J^{(n)}(x,y) = 0$, the steady-state solution of Eq. (11), obtained by setting $g^{(n+1)} = g^{(n)} = g$, is $g(x,y) = g_s(x,y)$, that is, the gain recovers to the small-signal value as it should. To further explore the gain model, we consider the case that the gain $g^{(n)}$ is close to unity and ignore any spatial dependence. In the steady state then, we find the approximate gain formula

$$g \approx \frac{g_s}{\left[1 + \frac{(f_{\rm rep}\tau)J}{J_{\rm sat}}\right]}. \tag{12}$$

This limit yields gain saturation of the expected form, though the intracavity fluence J is multiplied by a factor $(f_{\rm rep}\tau) = \tau/T$. Because the upper state lifetime of the laser transition τ is much greater than the cavity round-trip time T, the fluence appearing in the saturation formula is accumulated over $(f_{\rm rep}\tau)$ round trips. For our simulations, we employ the full Frantz-Nodvik model in Eq. (11), but the approximation in Eq. (12) serves to elucidate the nature of the gain model.

For our simulations, we employed the gain model of Eq. (11) in conjunction with the cavity field mapping in Eq. (2) to obtain the steady-state solution for the intracavity field $E(x,y)$, and then Eq. (9) is employed to obtain the average output power. The cavity propagation described by the generalized Huygens integral in Eq. (3) is performed using standard Fourier-transform methods on a square grid.

C. Laser threshold

The final ingredient of our model involves the properties of the gain medium described by the small-signal gain in Eq. (10), with peak gain g_0 and gain spot size w_p. This step requires determining the value of the on-axis small-signal gain $g_0 = g_{\rm th}$ required to achieve laser threshold for a given output coupler reflectance R. To find this value, we need the small-signal net power gain $G = e^g$ for the Gaussian mode of the cavity. In our simulations, we see little distortion of the cavity field from the Gaussian mode, so we may estimate the net power gain by averaging the small-signal power gain e^{g_s} over the

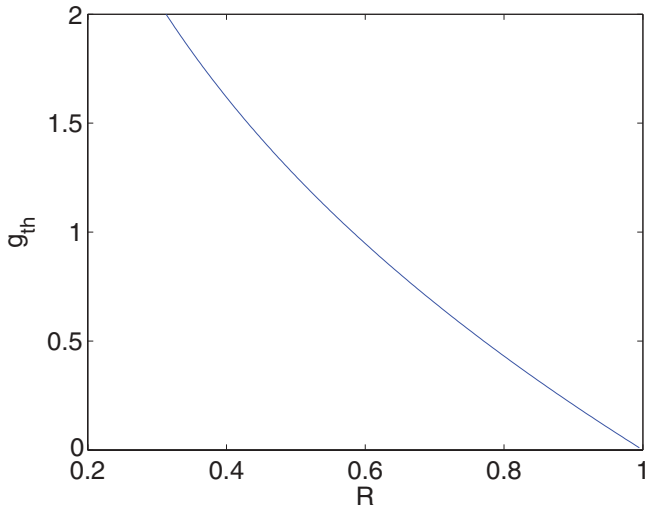

FIG. 2. (Color online) Threshold gain g_{th} as a function of R calculated using Eq. (15).

Gaussian-mode profile,

$$e^g = \frac{\int_0^\infty 2\pi r dr e^{g_s(r)} e^{-2r^2/w_0^2}}{\int_0^\infty 2\pi r dr e^{-2r^2/w_0^2}}, \tag{13}$$

where $r = \sqrt{x^2 + y^2}$, and the small-signal gain $g_s(r) \equiv g_s(x,y)$ is given by Eq. (10). As shown in the Appendix, for the case $w_p = w_0$, this integral can be evaluated to yield

$$G = e^g = \frac{1}{g_0}(e^{g_0} - 1). \tag{14}$$

This result holds if the pump-beam spot size matches the Gaussian-mode size at the gain medium as in the experiment. The simulations presented here operate in this regime, though the effect of varying the pump spot size is studied separately in Sec. IV C. Setting $g_0 = g_{\text{th}}$ in the threshold condition $GR = 1$ yields the relation

$$\frac{g_{\text{th}}}{(e^{g_{\text{th}}} - 1)} = R, \tag{15}$$

which can be used to obtain the on-axis small-signal gain g_{th} required for laser threshold with a given R. We have found that over a large range of experimentally relevant parameters, the threshold condition in Eq. (15) works very well. Figure 2 shows the calculated threshold gain as a function of R. For example, for the fs amplifying cavities studied here, we have $R = 0.66$ which yields $g_{\text{th}} = 0.78$. Furthermore, hereafter we specify $g_0 = \eta g_{\text{th}}$ using the parameter $\eta \geqslant 0$, which stipulates how far above (or below) threshold the laser is operating. From this, it follows that η can be written in the alternate forms

$$\eta = \frac{g_0}{g_{\text{th}}} = \frac{P_{\text{pump}}}{P_{\text{th}}}, \tag{16}$$

where P_{pump} is the pump power and P_{th} is the threshold pump power. This is a useful approach to specifying the peak small-signal gain via η as the threshold pump power P_{th} is experimentally accessible.

IV. OPERATING CHARACTERISTICS

A. Amplified output

In this section, we compare the results of our simulations against results from our in-house experiment as a means to validate our injection-locking model. Quantities of particular interest are the average output power versus the pump-beam power for both the 50 MHz and 100 MHz fsAC cavities, and the amplification G_{out} given by the net power gain of the output frequency comb compared to the input,

$$G_{\text{out}} = \frac{P_{\text{out}}}{P_{\text{in}}}. \tag{17}$$

For our simulations, we chose $J_{\text{sat}} = 1.25\ \text{J/cm}^2$, $\tau = 2.6\ \mu\text{s}$, and $P_{\text{th}} = 3.1$ W. This value of the saturation fluence J_{sat} agrees with previously measured values [6,7], and the threshold pump power $P_{\text{th}} = 3.1$ W was determined experimentally, and allows us to parametrize the level above threshold $\eta = P_{\text{pump}}/P_{\text{th}}$. The value $\tau = 2.6\ \mu$s for the upper state lifetime is compatible with a temperature rise of a few tens of degrees in the laser medium due to the pump beam [8,9], and is consistent with the conditions of the experiment. In spite of this implied temperature rise, we have been able to successfully model the fsAC without including the effects of thermal lensing.

Figure 3 shows the average power P_{out} of the output frequency comb versus pump power P_{pump} for the cases of (a) the 50 MHz fsAC with an average input power of $P_{\text{in}} = 0.54$ W, and (b) the 100 MHz fsAC with an average input power of $P_{\text{in}} = 0.86$ W. In each case, there is excellent agreement between the solid line showing the simulated output power and the crosses marking experimental values. In terms of the net power gain, the 100 MHz fsAC with $P_{\text{in}} = 0.86$ W yields $G_{\text{out}} = 7.8$, in good agreement with the experiment of Ref. [1]. It is a testimony to the utility of the model that it works so well for both fsAC cavities with different input powers. In particular, according to Eq. (11), the gain recovery dynamics,

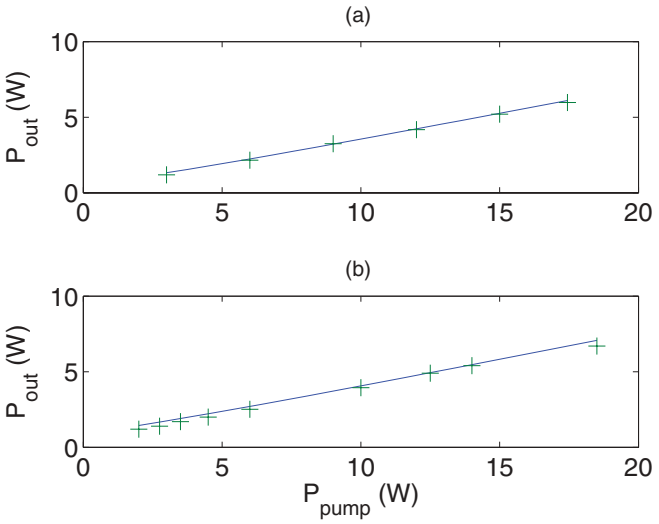

FIG. 3. (Color online) Output power P_{out} vs pump power P_{pump} for (a) the 50 MHz fsAC using $P_{\text{in}} = 0.54$ W, and (b) the 100 MHz fsAC with $P_{\text{in}} = 0.86$ W. The solid lines correspond to the results of the simulation and the crosses mark the experimental data. The horizontal axis is the same in both plots.

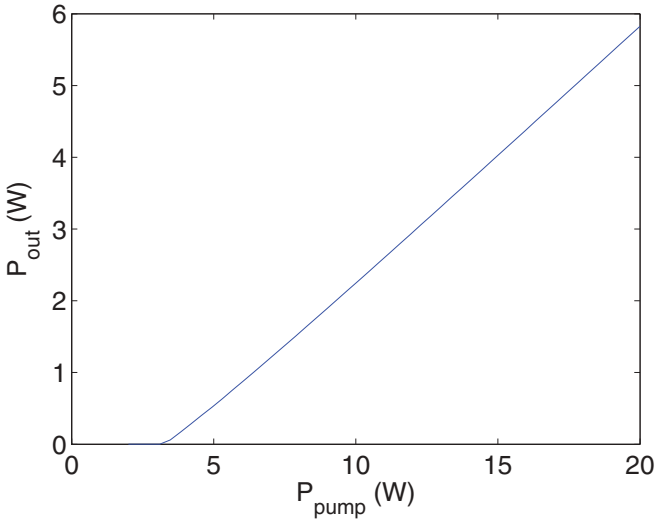

FIG. 4. (Color online) Simulated free-running output power P_{out} vs pump power P_{pump} for the 50 MHz fsAC.

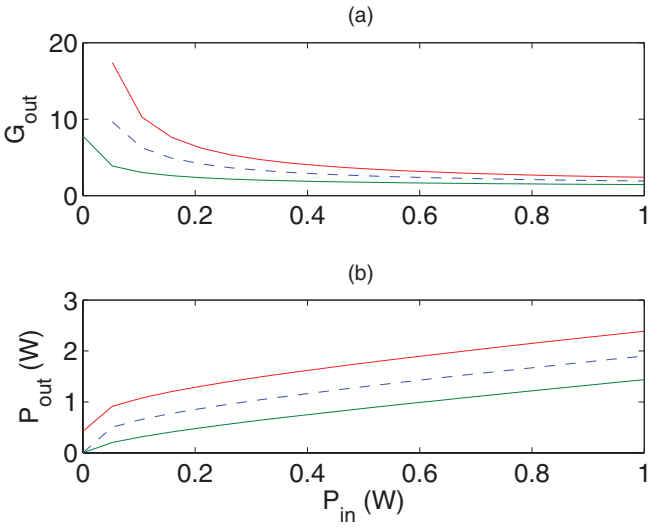

FIG. 5. (Color online) For the case of the 50 MHz fsAC, the plots are (a) the amplification G_{out} vs average input power P_{in}, and (b) the output power P_{out} vs average input power P_{in}. In each plot, the curves from bottom to top are for $\eta = 0.5, 1, 1.5$, with the dashed line corresponding to threshold with $\eta = 1$. The horizontal axis is the same in both plots.

and hence gain saturation, will be significantly different for the $f_{\text{rep}} = 50, 100$ MHz cavities.

Our model can also predict the free-running laser properties of the fsAC by taking the limit $P_{\text{in}} \to 0$ with no injection. Figure 4 shows the output power versus pump power for the free-running 50 MHz fsAC. This figure clearly shows the laser threshold at $P_{\text{pump}} = P_{\text{th}} = 3.1$ W, and also predicts P_{out}=5.1 W for $P_{\text{pump}} = 18$ W, with excellent experimental agreement. We find similar agreement for the case of the 100 MHz fsAC.

The results presented provide validation of our simulation model against experiment. In the remainder of this paper, we shall concentrate on the 50 MHz fsAC cavity as an illustrative example, though very similar results are obtained for the 100 MHz case.

B. Below and above threshold

Having now validated our cavity model to a reasonable degree, we turn to exploring some operating characteristics of the 50 MHz fsAC. One question that arises is whether there is any great benefit from operating the fsAC above threshold $\eta > 1$. In particular, gain saturation will generally reduce the net gain down close to threshold, thereby potentially erasing any benefit of working above threshold. To address this issue, Fig. 5(a) shows a plot of the amplification G_{out} versus average input power P_{in}, and Fig. 5(b) shows the output power P_{out} versus P_{in}. In each plot, the curves from bottom to top are for $\eta = 0.5, 1, 1.5$, with the dashed line corresponding to threshold with $\eta = 1$. Figure 5(a) clearly illustrates that there is always a greater amplification above threshold in comparison to below threshold, but as the input power is increased, the amplifications for above and below threshold approach the value at threshold (dashed line). In general, there is always a benefit in the attainable amplification by working above threshold, though this can be lessened at higher input powers. Figure 5(b) shows the output power versus input power corresponding to Fig. 5(a). Here we again see that there is a decided advantage to working above threshold in terms of the output power, even for larger input powers.

C. Variation with pump beam

Next we examine the robustness of the operation of the fsAC cavity against variations in the pump beam. In general, extreme measures are taken to align the input beam with the cavity axis; however, the pump beam may be misaligned or have a spot size differing from the assumed condition $w_p = w_0$. To examine the effects of such variations in the pump beam, we extend the small-signal gain expression in Eq. (10) to

$$g_s(x,y) = g_0 e^{-2[(x-x_0)^2+y^2]/w_p^2}, \tag{18}$$

with x_0 being the misalignment of the pump beam along the x axis, w_p being the pump-beam spot size, and g_0 being the peak small-signal gain that will be proportional to the peak pump-beam intensity, $I_p = P_{\text{pump}}/(\pi w_p^2/2)$. In order to conduct a comparative study, we consider the case of a fixed pump-beam power so that g_0 and w_p are varied in such a way that $g_0 w_p^2 = (\eta g_{\text{th}}) w_0^2$ remains constant. In particular, here we consider the practically relevant case of the 50 MHz fsAC with $P_{\text{in}} = 0.54$ W and parameters as in Fig. 3.

Figure 6 shows the variation of the output power P_{out} versus the normalized pump spot size w_p/w_0. A key feature is that for $w_p/w_0 > 1$, the output power decreases, albeit not rapidly, indicating a robustness against variations in pump spot size. In contrast, for $w_p/w_0 < 1$, the output power initially increases with decreasing pump spot size. However, for $w_p/w_0 < 0.67$, no steady-state solution for the cavity-mode equations is found—numerically indicating the onset of an instability. That is, the intracavity field does not approach a state for which $|E^{(n+1)}(x,y)|^2 = |E^{(n)}(x,y)|^2$. Although our cavity model is incapable of diagnosing the full nature of the instability since we have neglected cavity dispersion and associated time dynamics, the appearance of the instability signals that the output pulse train will no longer simply be an amplified version of the input pulse train. The consequence of this is that the

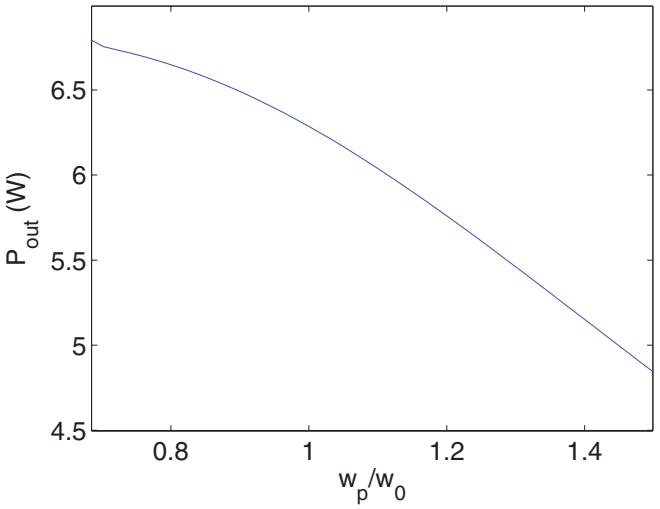

FIG. 6. (Color online) Output power P_{out} vs the normalized pump spot size w_p/w_0 for the 50 MHz fsAC with an input power of $P_{\text{in}} = 0.54$ W. For $w_p/w_0 < 0.67$, a steady-state solution is not obtained, indicating that the fsAC is unstable in this regime.

fsAC will no longer act as a successful amplifier for infrared frequency combs. Our main message from these simulations is that although the details depend on the specific parameters for the fsAC, we have found that the choice of pump spot size $w_p/w_0 = 1$ provides a reliable operating point for fsAC operation, with ample room for variations in the pump spot size to allow for stable operation.

For a second set of simulations, we have considered the same fsAC parameters as above with $w_p/w_0 = 1$ and varied the normalized beam displacement x_0/w_0 of the pump beam. The results displayed in Fig. 7(a) show the output power P_{out} versus the normalized pump beam displacement x_0/w_0, and Fig. 7(b) shows the beam quality factors M_x^2 (solid line) and M_y^2 (dashed line) along the two transverse directions versus x_0/w_0. Figure 7(a) clearly shows that pump-beam misalignment leads to a degradation of the output power. On the other hand, the reduction in output power is only $\simeq$10% for a pump-beam misalignment of half the pump-beam spot size $x_0 = w_p/2$, reflecting a very high degree of robustness against misalignments. Very similar results were obtained for the 100 MHz fsAC cavity.

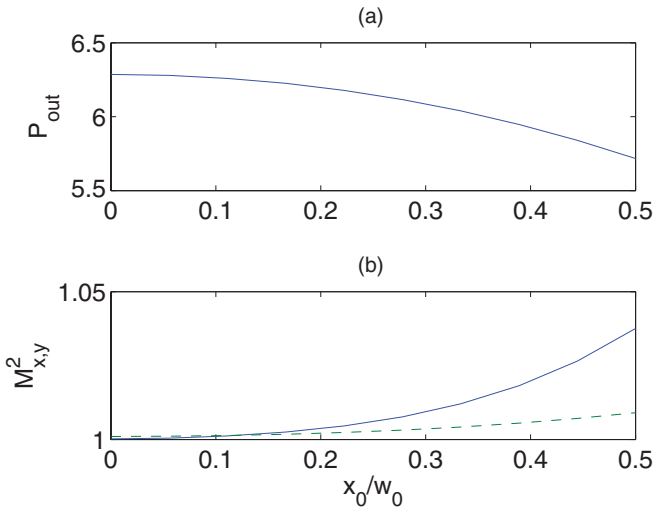

FIG. 7. (Color online) For the case of the 50 MHz fsAC with an input power of $P_{\text{in}} = 0.54$ W, the plots are (a) the output power P_{out} vs the normalized pump-beam displacement x_0/w_0, and (b) the beam quality factors M_x^2 (solid line) and M_y^2 (dashed line) along the two transverse directions vs x_0/w_0. The horizontal axis is the same in both plots.

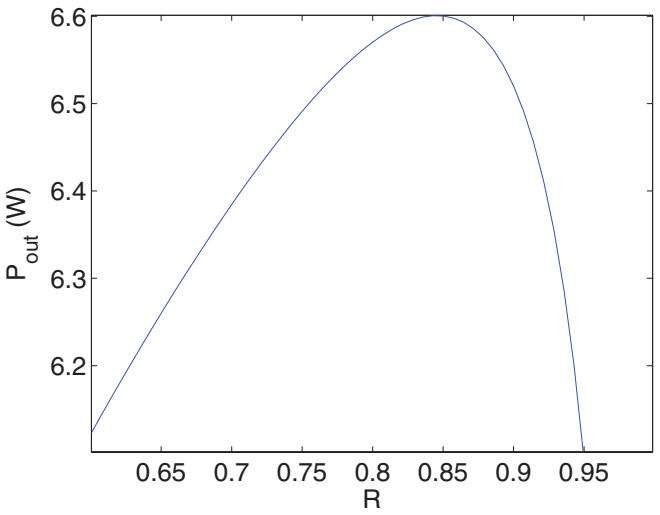

FIG. 8. (Color online) Output power P_{out} vs the reflectance R of the output coupler for the case of the 50 MHz fsAC with an input power of $P_{\text{in}} = 0.54$ W.

Figure 7(b) shows the corresponding variation in the beam quality factor $M_{x,y}^2$ along the x and y axis as a function of w_p/w_0. The beam quality factor M^2 provides a measure of the quality of the output beam from the fsAC with respect to the input Gaussian beam having $M_{x,y}^2 = 1$ [10]. It is noteworthy that the output beam quality factors for the current fsAC design remain very close to unity for pump-beam misalignments as large as $x_0 = w_p/2$, again reflecting the remarkable robustness of the cavity.

D. Variation with output coupler

We close this section with an investigation of whether the average output power may be usefully increased by varying the reflectance R of the output coupler. Figure 8 shows the output power P_{out} versus R for the case of the 50 MHz fsAC with an input power of $P_{\text{in}} = 0.54$ W. While the current experimental setup uses $R = 0.66$ with output power $\simeq$6.3 W, the figure indicates that the output power can be increased by approximately 5% to 6.6 W using $R = 0.85$. In the next section, we shall see that such an increase may be offset by a decrease in the attainable injection-locking range.

V. INJECTION-LOCKING RANGE

A. Locking range

In this section, we investigate the injection-locking range of the 50 MHz fsAC with a pump power of $P_{\text{pump}} = 18$ W. The results from Fig. 4 yield a free-running output power of $P_{\text{out}} = P_{\text{fr}} = 5.1$ W for this cavity. For the purposes of this

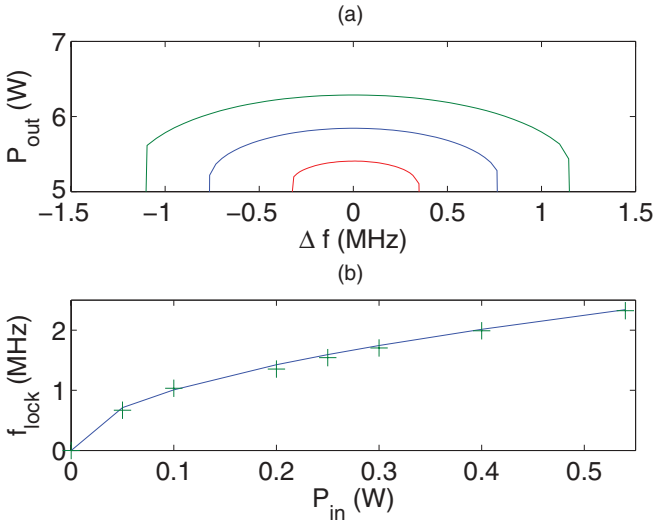

FIG. 9. (Color online) (a) Average output power P_{out} as a function of frequency detuning Δf. The input powers for the curves (from top to bottom) are $P_{\text{in}} = 0.54, 0.25, 0.05$ W. Note: the output power is set to zero when no stable solution is found. (b) Frequency locking range f_{lock} vs input power P_{in}.

analysis, we vary the round-trip phase shift in Eq. (5) away from resonance by allowing $\phi_L = 2\pi\Delta f T = 2\pi\Delta f/f_{\text{rep}}$ to be nonzero, with Δf being the frequency detuning from a longitudinal cavity resonance. Figure 9(a) shows the average output power P_{out} as a function of frequency detuning Δf. The input powers used for the curves (from top to bottom) are given by $P_{\text{in}} = 0.54, 0.25, 0.05$ W. A key finding of these simulations is that a stable intracavity field occurs only over a restricted range of frequency detunings around resonance at $\Delta f = 0$. For ease of viewing, in Fig. 9(a), we set the output power to zero for detunings at which the field solution is unstable. The injection-locking range f_{lock} is, then, the range over which the output power shown is nonzero. Figure 9(a) further illustrates that for a given input power, the peak output power occurs for zero detuning, and that the output power decreases with decreasing input power and approaches the free-running output power of $P_{\text{fr}} = 5.1$ W for small input powers (see the lower curve for $P_{\text{in}} = 0.05$ W). Finally, it also demonstrates that the locking range decreases with decreasing input power. These features coincide with general expectations for the injection-locking range even for continuous-wave operation [11].

The crosses in Fig. 9(b) show the frequency locking range f_{lock} versus input power P_{in} obtained from the numerical simulations, with the solid line showing a fit to the data. It is interesting to compare this with theory for single-mode lasers, which predicts the frequency locking range as [11]

$$f_{\text{lock}} = \frac{2(1-R)f_{\text{rep}}}{\pi}\sqrt{\frac{P_{\text{in}}}{P_{\text{fr}}}}. \tag{19}$$

Using the relevant experimental values, this formula yields $f_{\text{lock}} = 4.8\sqrt{P_{\text{in}}}$ MHz. Performing a numerical fit to the data in Fig. 9(b) gives the same functional dependence as Eq. (19), but with a modified overall multiplier: $f_{\text{lock}} = 6.4\sqrt{P_{\text{in}}}$ MHz. Although the injection-locking theory for single-mode lasers is not strictly valid for the present system, it is interesting to note the similarity between the systems. Theoretical predictions for injection locking in mode-locked systems also share the square-root dependence on the injected power [12]. Our simulations therefore comply with general expectations regarding the locking range of the fsAC [11]. In particular, we note that the predicted injection-locking range in Eq. (19) decreases with increasing reflectance R of the output coupler. Thus, in comparison to the case of $R = 0.66$ used here, the increase in output power for $R = 0.85$ indicated in Fig. 8 will lead to a concomitant smaller locking range—an important tradeoff when considering fsAC design.

B. Limitations for short pulses

Because cavity dispersion has been neglected in this treatment, the results obtained thus far are independent of the input pulse duration t_p. This is reflected in the fact that the gain saturation of the Ti:sapphire amplifying medium depends only on the circulating pulse fluence and not on the peak pulse intensity, $I(x,y) = |E(x,y)|^2/t_p$. However, due to the nonlinear Kerr effect [13] in the Ti:sapphire medium, with nonlinear coefficient $n_2 = 3\times10^{-16}$ cm^2/W [14], the cavity dynamics can become intensity dependent for shorter pulse durations. While the approach in the previous sections has tacitly dealt with the long pulse limit, we next elucidate how the pulse duration enters the picture.

To incorporate the Kerr effect into the cavity model in Eq. (2), we generalize the round-trip phase shift to include a nonlinear, intensity-dependent term that depends on the round trip n according to

$$\phi \to \phi^{(n)}(x,y) = -\phi_G + \phi_L + \frac{k_0 n_2 L|E^{(n)}(x,y)|^2}{t_p}, \tag{20}$$

with $L = 6$ mm the gain medium length. Figure 10 shows the average output power P_{out} including the nonlinear Kerr effect as a function of frequency detuning Δf for $P_{\text{in}} = 0.54$ W.

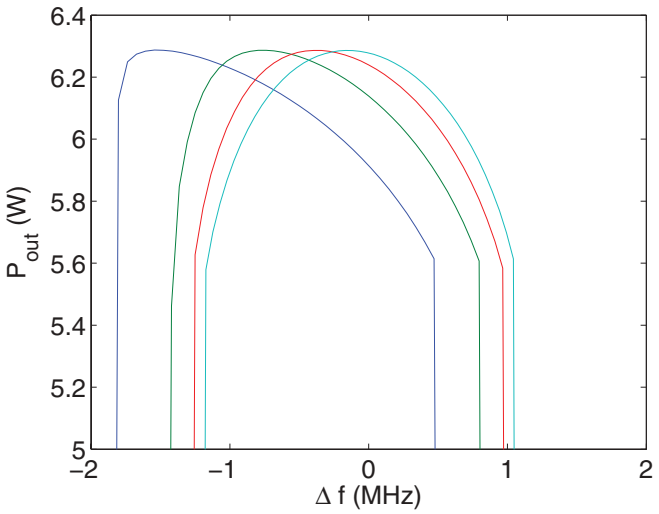

FIG. 10. (Color online) Average output power P_{out} including the nonlinear Kerr effect as a function of frequency detuning Δf. From the farthest left curve and moving to the right, the corresponding pulse durations are $t_p = 5, 10, 20, 50$ ps. The output power is set to zero when no stable solution is found.

Again, for ease of viewing, we have set the output power to zero for detunings where the field solution is unstable. Starting from the farthest left curve and moving to the right, the corresponding pulse durations are $t_p = 5,10,20,50$ ps. For the longest pulse duration $t_p = 50$ ps, the curve of P_{out} versus Δf in Fig. 10 is very close to the corresponding curve for $P_{\text{in}} = 0.54$ W in Fig. 9(a), whereas the remaining curves for shorter pulse durations are clearly shifted to the left in addition to becoming increasingly asymmetric with reducing pulse duration. This implies that the nonlinear Kerr effect comes into play for pulse durations $t_p < 50$ ps. Furthermore, we note from Fig. 10 that the frequency detuning Δf of peak output power shifts and becomes more negative with decreasing pulse duration. This arises from the fact that as the pulse duration is decreased and the nonlinear phase shift due to the Kerr effect increases, a larger negative frequency detuning is required to maintain overall cavity resonance. It is noteworthy, however, that as the input pulse duration is decreased, the output power at the position of the peaks in Fig. 10 stays essentially the same—implying that decreasing pulse duration does not sacrifice average output power. Indeed, the relative insensitivity of the peak output power to the Kerr effect means that the results in Figs. 3–8 are little changed by the Kerr effect for $t \geqslant 5$ ps.

We conclude by pointing out that the Kerr effect imposes a very real and practical limitation to the frequency comb pulse duration that can be successfully amplified in the fsAC. In particular, it is a practical reality that the cavity length of the fsAC fluctuates with time and to deal with this a servo is used to dynamically adjust the cavity length in such a way as to maximize the output power. What this means is that the fsAC strives to work at the peak of tuning curves shown in Fig. 10. For long pulse durations, the peak is well pronounced with stable regions on both sides that can accommodate fluctuations around the peak. However, we see that already for $t_p = 5$ ps, the tuning curve has become very asymmetric with a large stable region on the right side of the peak, but a smaller stable region on the left side. For $t_p < 5$ ps, this asymmetry becomes more pronounced with the operating point at the detuning of peak output power becoming ever closer to the unstable region on the left of the tuning curve. This means that for $t_p < 5$ ps, there is little flexibility to accommodate unavoidable fluctuations in the cavity detuning and this puts a limitation to the pulse duration that can be stably amplified by the fsAC. Our simulations imply that the minimum pulse duration is $t_p = 2$ ps for our particular fsAC design.

VI. SUMMARY AND CONCLUSIONS

In summary, we have developed a cavity model including transverse field variations and gain saturation in the Ti:sapphire gain medium to elucidate the operating characteristics of a femtosecond amplification cavity with an incident infrared frequency comb. We found excellent agreement between our simulations and experiment for the case of input pulses of 5 ps duration and we explored operating characteristics such as the output power and injection-locking range. For shorter input pulses, however, our simulations indicate that the nonlinear Kerr effect will become a key player, in addition to temporal effects related to cavity dispersion. In the near future, we will report on an extended version of this model to address temporal aspects such as the effect of pulse chirp and intracavity dispersion on the performance of the fsAC.

ACKNOWLEDGMENTS

This work is supported in part by the AFOSR Grant No. FA9550-12-1-0048. D.R.C. acknowledges support from the TRIF photonic graduate student support program.

APPENDIX: THRESHOLD GAIN

We start from Eq. (13),

$$G = e^g = \frac{\int_0^\infty 2\pi r dr e^{g_s(r)} e^{-2r^2/w_0^2}}{\int_0^\infty 2\pi r dr e^{-2r^2/w_0^2}}. \tag{A1}$$

For the specific case $w_p = w_0$, the term $e^{g_s(r)}$ in the integral in the numerator can be Taylor expanded as

$$g_s(r) = e^{g_0 e^{-2r^2/w_0^2}} = \sum_{j=0}^{\infty} \frac{g_0^j}{j!} e^{-2jr^2/w_0^2}. \tag{A2}$$

Substituting Eq. (A2) into (A1) and performing the integrals yields

$$\begin{aligned} G &= \sum_{j=0}^{\infty} \left(\frac{g_0^j}{j!}\right) \frac{\int_0^\infty 2\pi r dr e^{-2r^2(1+j)/w_0^2}}{\int_0^\infty 2\pi r dr e^{-2r^2/w_0^2}} \\ &= \sum_{j=0}^{\infty} \left(\frac{g_0^j}{j!}\right) \frac{1}{(1+j)} = \frac{1}{g_0} \sum_{j=1}^{\infty} \left(\frac{g_0^j}{j!}\right) = \frac{1}{g_0}(e^{g_0} - 1), \end{aligned} \tag{A3}$$

which is the desired result.

[1] J. Paul, J. Johnson, J. Lee, and R. J. Jones, Opt. Lett. **33**, 2482 (2008).
[2] J. Lee, D. R. Carlson, and R. J. Jones, Opt. Express **19**, 23315 (2011).
[3] See, A. E. Siegman, *Lasers* (University Science Books, Herndon, VA, 1986), Chap. 15.
[4] See, A. E. Siegman, *Lasers* (University Science Books, Herndon, VA, 1986), Chap. 20.
[5] L. M. Frantz and J. S. Nodvik, J. Appl. Phys. **34**, 2346 (1963).
[6] S. Takeuchi and T. Kobayashi, Opt. Commun. **109**, 518 (1994).
[7] F. Estable, F. Salin, M. Allain, P. Georges, and A. Brun, Opt. Commun. **72**, 235 (1989).
[8] R. C. Powell, G. E. Venikouas, L. Xi, and J. K. Tyminski, J. Chem. Phys. **84**, 662 (1986).
[9] P. Albers, E. Stark, and G. Huber, J. Opt. Soc. Am. B **3**, 134 (1989).
[10] See, for example, A. E. Siegman, in *DPSS (Diode Pumped Solid State) Lasers: Applications and Issues*, edited by M. Dowley, OSA trends in Optics and Photonics (Optical Society of America, Washington, DC, 1998), Vol. 17, paper MQ1.

[11] A. E. Siegman, *Lasers* (University Science Books, Herndon, VA, 1986), Chap. 29.

[12] N. Rebrova, G. Huyet, D. Rachinskii, and A. G. Vladimirov, Phys. Rev. E **83**, 066202 (2011).

[13] R. W. Boyd, *Nonlinear Optics*, 3rd ed. (Academic, New York, 2008), Chap. 4.

[14] A. Major, F. Yoshino, I. Nikolkaakos, J. Stewart Aitchison, and P. W. E. Smith, Opt. Lett. **29**, 602 (2004).